New insights into the physics of inertial microfluidics in curved microchannels. I. Relaxing the fixed inflection point assumption

View Online   Export Citation   CrossMark

Mehdi Rafeie,[1,a)] [ID] Shahin Hosseinzadeh,[1] [ID] Robert A. Taylor,[1,2] [ID] and Majid Ebrahimi Warkiani[3,4]

AFFILIATIONS

[1]School of Mechanical and Manufacturing Engineering, University of New South Wales, Sydney, New South Wales 2052, Australia
[2]School of Photovoltaic and Renewable Energy Engineering, University of New South Wales, Sydney, New South Wales 2052, Australia
[3]School of Biomedical Engineering, University of Technology Sydney, Sydney, New South Wales 2007, Australia
[4]Institute of Molecular Medicine, Sechenov First Moscow State University, Moscow 119991, Russia

[a)]Author to whom correspondence should be addressed: mehdi.rafeie@unsw.edu.au.

ABSTRACT

Inertial microfluidics represents a powerful new tool for accurately positioning cells and microparticles within fluids for a variety of biomedical, clinical, and industrial applications. In spite of enormous advancements in the science and design of these devices, particularly in curved microfluidic channels, contradictory experimental results have confounded researchers and limited progress. Thus, at present, a complete theory which describes the underlying physics is lacking. We propose that this bottleneck is due to one simple mistaken assumption—the locations of inflection points of the Dean velocity profile in curved microchannels are not fixed, but can actually shift with the flow rate. Herein, we propose that the dynamic distance (δ) between the real equilibrium positions and their nearest inflection points can clearly explain several (previously) unexplained phenomena in inertial microfluidic systems. More interestingly, we found that this parameter, δ, is a function of several geometric and operational parameters, all of which are investigated (in detail) here with a series of experiments and simulations of different spiral microchannels. This key piece of understanding is expected to open the door for researchers to develop new and more effective inertial microfluidic designs.

I. INTRODUCTION

"Microfluidic" technology was born in 1992 with the fabrication of a microchiplike structure which enabled its pioneers to study electrophoresis in a controlled, miniaturized device.[1] Compared to conventional macroscale platforms, this technology provided reduced reagent volumes, fast sample processing, low cost, high sensitivity, and improved portability.[2] Among existing microfluidic systems, inertial microfluidics has experienced massive growth in the past two decades, particularly for cell sorting applications.[3,4] In these systems, suspended cells/particles flowing in a microchannel migrate laterally under the influence of hydrodynamic lift forces which are proportional to particle size and the fluid's mean shear gradient. This phenomenon is known as inertial migration of particles.

In 2004, Matas *et al.*[5] elucidated previously developed theories asserting that the net inertial lift force, F_{Net}, is comprised of two components: (1) a shear gradient lift force, F_S, that pushes particles down the gradient of the shear rate, $\dot{\gamma}$, and, (2) a wall-induced lift force, F_W, which always pushes particles away from the wall toward the channel centerline. These forces, then, balance at an equilibrium position between the channel wall and the centerline. In 2007, Di Carlo *et al.*[6] conducted some of the seminal work in inertial microfluidics, which involved utilizing the aforementioned forces on the scale of microchannels, where both inertia and viscosity are equally important. Two years later, he performed finite element simulations for particles in square channels to determine the distribution of lift forces in the cross section of the microchannels and to consider focusing in three-dimensional (3D) flows.[7,8]

In 2013, Zhou and Papautsky[9] presented a two-stage model for the inertial focusing: Stage 1—Particles migrate near channel walls due to the vorticity around the particles' surface as the origin of both F_W and F_S; Stage 2—Once an initial equilibrium is reached, a rotation-induced lift force, F_Ω, becomes dominant and drags particles to the center point of all four of the channel walls. This second focusing stage well explained the occurrence of four stable equilibrium positions in a square microchannel, and two equilibrium positions near the longer walls of a rectangular microchannel with low or high aspect ratios (AR), an occurrence which had been previously observed experimentally and exploited by different research groups.[10,11]

In addition to the inertial lift forces in straight channels, the introduction of curvature to a channel induces another degree of freedom through centrifugal effects that can be employed to further manipulate inertial focusing. This type of secondary flow was first studied theoretically by Dean[12] in 1927. In 2014, Ramachandraiah et al.[13] systematically analyzed Dean drag forces, F_D, to show that randomly distributed particles entering a curved channel can be focused to a fixed lateral position exiting the curvature regardless of the radius of the curvature and—importantly—the initial position of the particles. In 2017, Nivedita et al.[14] showed that at relatively high Reynolds numbers, e.g., $Re > 100$, multiple Dean vortices are presented in curved channels—a phenomenon which was further investigated by other researchers.[15–17]

Along these lines, many different microdevices have recently been designed to take advantage of secondary flow, including topologically patterned microchannels,[18] serpentines,[19–21] contraction/expansion arrays,[22,23] and micropillar structures.[24] As an early example, in 2007, Seo et al.[25] reported a double rectangular spiral microchannel that could focus $10.5\,\mu m$ particles near the inner wall of the channel. Since then, spiral inertial microfluidic systems have continued to gain prominence, becoming the most commonly researched microstructure for filtration and separation applications today.[26]

As spiral microchannel designs have matured, they have also been extended to include different cross sections. In 2012, Martel and Toner[27] reported that by lowering the aspect ratio of rectangular spiral microchannels, the width and the position of the inertial focusing bands become more dependent on the flow rate. Wu et al.[28] introduced a novel trapezoidal cross section spiral microchannel for the separation of leukocytes from blood, which generated stronger Dean vortices in the outer half of the channel. In 2013, Guan et al.[29] reported that particles underwent an abrupt shift from the inner side of a trapezoidal microchannel to its outer side at a size-dependent critical flow rate. This phenomenon allowed them to controllably fractionate particles/cells with a higher resolution compared to rectangular channels. In 2014, Warkiani et al.[30] utilized a slanted spiral microchannel to achieve label-free isolation of circulating tumor cells with a purity of >80%. This group then developed a multiplexed platform to boost the throughput and utilized it for membrane-less Chinese Hamster Ovary (CHO) cells and yeast cells filtration[31] as well as for blood plasma separation.[32]

Despite this great potential of spiral inertial microfluidic technology for many important applications,[33] there remain a few critical unexplained phenomena in inertial microfluidics. For example, when Guan et al.[29] comparatively analyzed rectangular and trapezoidal

spiral microchannels, their force analysis indicated that in the outer half of spiral microchannels, F_{Net} and F_D are generally in the same direction and, therefore, it is not theoretically possible for particles to focus, contrary to their experimental observations. Even though the work of Guan et al. represents considerable progress in the field, the underlying mechanisms of inertial focusing cannot be fully explained by their theory. As another example, several researchers[28–32,34] have observed—but not explained—a sudden jump of particles from a focusing position in the inner half to another in the outer half of trapezoidal spiral channels. Lastly, the slope direction of a slanted channel (e.g., inward sloping[32,35] or outward sloping[3,29]) clearly plays an important role in particle focusing position, but this aspect has not yet been addressed in terms of how slope impacts the pattern of secondary flow. In the following, we will explain these issues with a theory on how F_D and inertial lift forces may reach an equilibrium state at different locations in the cross section of a curved channel. Furthermore, we will investigate how inertial focusing mechanisms are influenced by the salient parameters, including flow rate, particle size, AR, wall slope, wall slope direction, flow direction, $\dot{\gamma}$ distribution, and Dean flow pattern.

II. EXPERIMENTAL

To systematically assemble a data set which showcases the full range of underlying physics (including the unexplained aspects) of inertial focusing in curved channels, we conducted a series of experiments on four rectangular ($R_{1–4}$), four outward sloping trapezoidal ($OT_{1–4}$), and four inward sloping trapezoidal ($IT_{1–4}$) microchannels with different aspect ratios and slopes. To expand this even further, each of these devices was tested over a wide range of flow rates (i.e., $Q = 0.5–9$ ml/min, $Re \simeq 20–450$) in two flow directions to reveal the effects of Re and Dean number, De, on inertial focusing. Figure 1 shows the details of the 12 microchannels considered in this research. Section 1 of the supplementary material provides the detailed geometric parameters of the channels.

Three differently-sized fluorescent particle suspensions (i.e., $a = 6$, 10, and $15\,\mu m$) at the same concentration were pumped in the forward direction (B-B to F-F) and in the backward direction (F-F to B-B) through the channels. In the forward flow, section F-F was observed from the top view only, while in the backward flow, section B-B was observed from the top and side views to literally (and figuratively) shed light on the focusing behavior of the microbeads. To observe particles flowing in the side view, the microchip was placed vertically under the microscope. Note that the gravitational forces in these microchips are negligible, regardless of orientation.[29,36]

III. RESULTS AND DISCUSSION

A. Inflection points of Dean flow

The location of the inflection points (IPs) of the secondary flow is of the utmost importance, since they determine how and where suspended particles focus in a curved microchannel. In contrast to the prevalent impression that the inflection points are fixed,[29,37–39] our results show that the locations of these points must be a function of multiple parameters, including Re, De, and geometry.
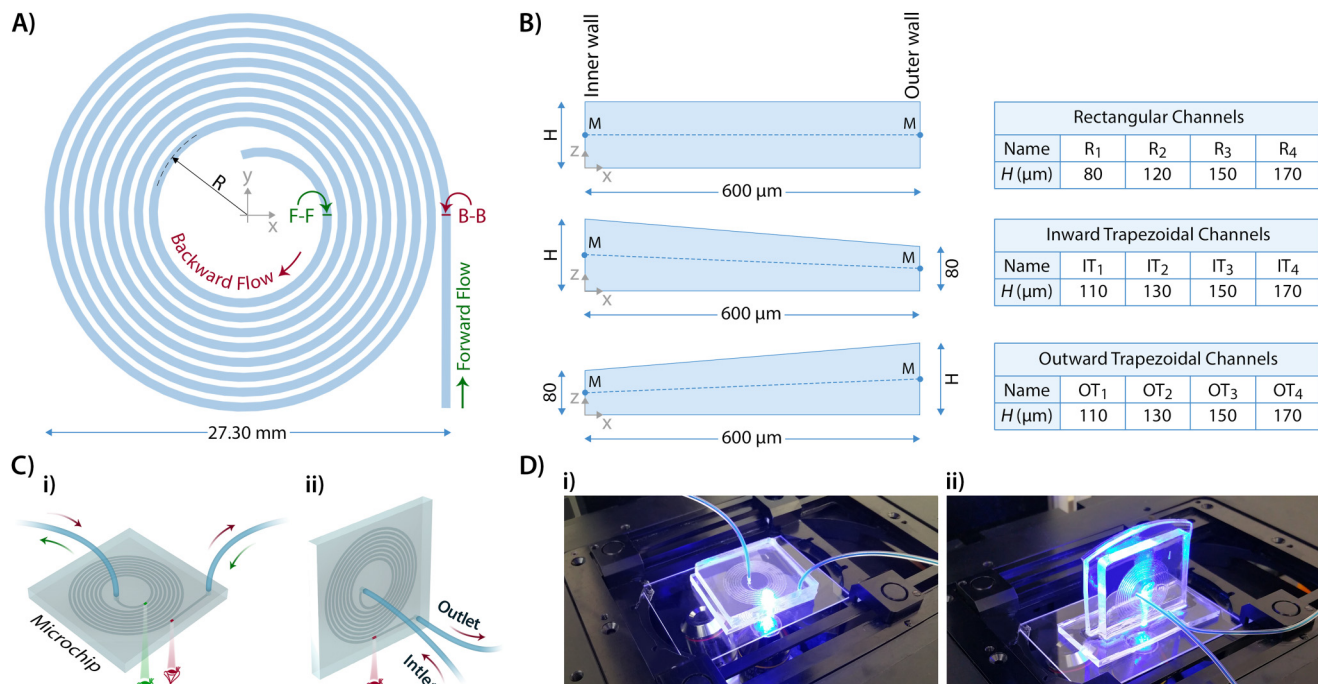
FIG. 1. Schematic of microchannels. (a) Top view of the spiral microchannels used in this study (i.e., the x–y plane). R indicates the radius of the channel curvature. Also, F-F and B-B denote sections of interest (near the outlet) in forward and backward flows, respectively. (b) Cross section of all channels in the x–z plane. The dashed "M-M" line designates the centerline of the cross section. (c) Schematic of the microchip for (i) top view observation in the forward (green) and backward (red) flows, and (ii) side-view observation in the backward flow. (d) Images of the experimental setup for an inverted microscope (i) top view and (ii) side view.

Figure 2(a) shows Computational Fluid Dynamics (CFD) simulation results of the Dean velocity vectors over the z axis centerline of the cross section of the channel R_1 at $Q = 6$ ml/min ($Re = 293$) in the backward flow. Each of the two inflection points (where $d^2 V_D/dz^2 = 0$) in the profile is located where the magnitude of the Dean velocity is zero (i.e., $V_D = 0$). In the literature, these points are referred to as "zero Dean velocity/flow" points. Figure 2(b) reveals that in the backward flow for the channel R_1, by increasing the flow rate from $Q = 0.5$ to 9 ml/min ($Re = 24$ to 440), the inflection points relocate as far as $12 \, \mu$m toward the M-M centerline of the cross section. Furthermore, we found that the secondary flow alters its direction along the x axis, while the z-component of the velocity vectors at the inflection points may not be necessarily zero. Therefore, the criterion for locating the inflection points must be defined as where $V_x = 0$ for accurate analysis of the pattern of Dean flow. Thus, for its mathematical precision, we will refer to these as "inflection points" rather than as "zero Dean velocity" points.

To speed up the analysis for finding these inflection points, in this work, we developed the "Dean flow analyzer" software to calculate and display the exact location of IPs in the cross section of a curved microchannel (for more information on the software applications developed in this work, see Sec. 2 of the supplementary material). The black-diamond symbols in Fig. 2(a) indicate IP locations calculated by this software application. To prove that the inflection points of the CFD profile coincide with the IPs

calculated by the software, an area around the upper inflection point is enlarged [Fig. 2(a)]. As can be seen in the figure, the computed IP is exactly located over the intersection point of the line obtained from the linear regression and the baseline of the Dean velocity profile. Figure 2(c) shows the computed locations of IPs in channels R_2, IT_2, and OT_2 at different flow rates. In the backward flow, the IP curves at low flow rates are close to the top and bottom walls. By increasing the flow rate, the IP curves move away from the walls. In the forward flow, however, the IP curves at low flow rates are close to the M-M centerline and approach the top and bottom walls as the flow rate increases.

B. Theoretical framework

Having scrutinized the numerical and experimental results of all the microchannels of this work, we concluded that it is possible to pull out three "commonalities" that govern the underlying physics of inertial focusing in curved microchannels. (1) Particles gradually approach the M-M centerline as the flow rate increases; (2) the distribution of high $- \dot{\gamma}$ regions corresponds to high magnitudes of F_W; (3) the cross section of a curved channel is divided into three regions which determine the force balance. In fact, these regions can be used to determine a key parameter, δ, which is proposed in this work and expresses the states of equilibrium positions in the cross section of the channel.
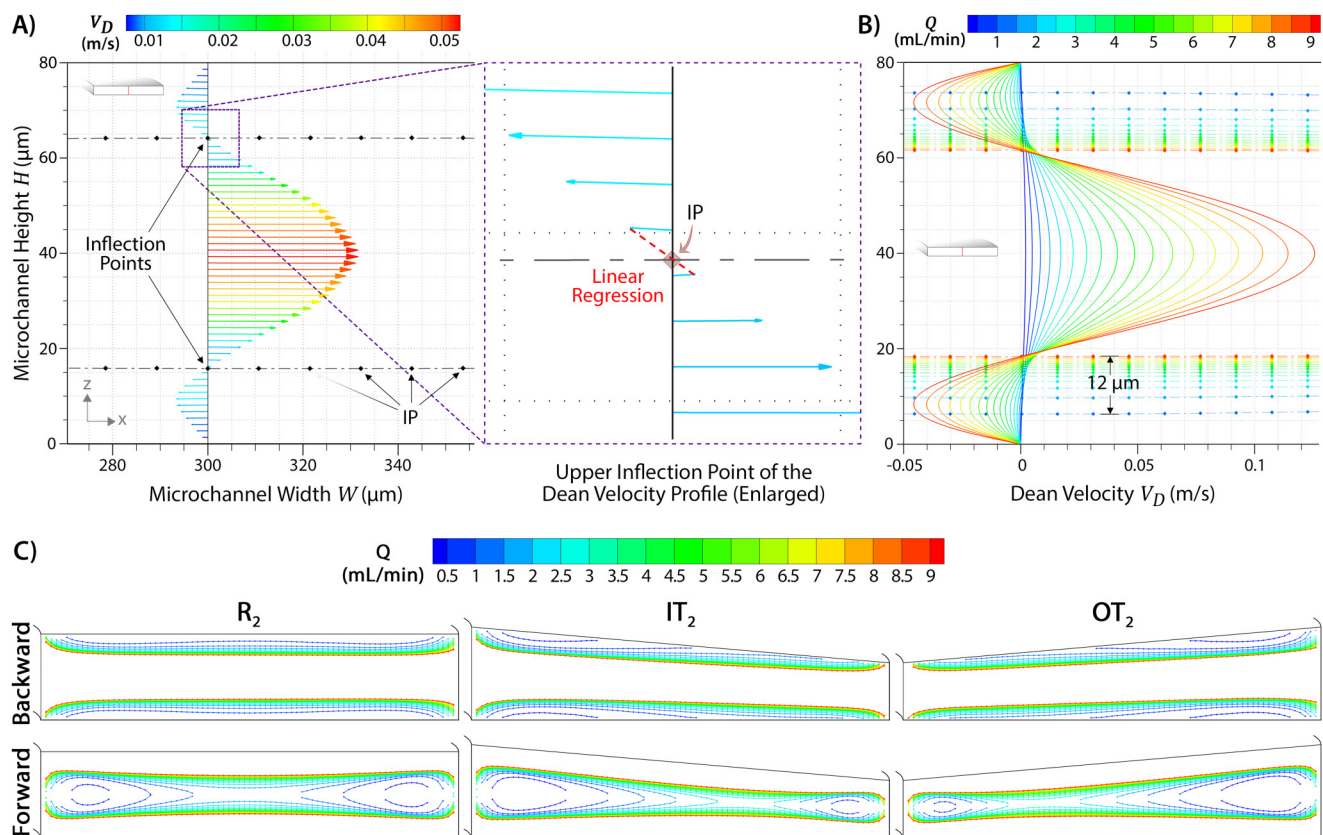
FIG. 2. Inflection points of the Dean flow. (a) Dean velocity vectors over a vertical line in the middle of the channel R_1 at $Q = 6$ ml/min in the backward flow (i.e., section B-B). An area around the upper inflection point is enlarged to show the exact location of the IP found by the "Dean flow analyzer" software. (b) Dean velocity profiles at $Q = 0.5$–9 ml/min over the same vertical line in the backward flow of the channel R_1. (c) Distribution of IPs at $Q = 0.5$–9 ml/min in the backward and forward flows in sections B-B and F-F of channels R_2, IT_2, and OT_2, respectively.

Although these commonalities can be elucidated abstractly, it is best to explain them along with numerical and experimental results. Therefore, the following sections will show that these commonalities hold for curved microchannels at least with low aspect ratios (e.g., $0.1 < AR < 0.3$) and within the range of $De < 40$.

C. Inertial focusing in rectangular curved channels

Figure 3(a) shows the experimental results of channels R_{1-4} accompanied by the focusing trends of microbeads shown in Fig. 3(b) (for more detail on image and video processing methods, see Secs. 3 and 4 of the supplementary material, respectively). Overall, in the rectangular spiral channels, particles focus near the inner wall at low flow rates, but move toward the outer half of the channel as the flow rate increases.

We define the sharpness factor of inertial focusing as $s = 1 - (b-a)/W$, where a is the particle diameter, b is the width of particle band, and W is the microchannel width. Therefore, a larger sharpness factor (i.e., as $s \to 1$) corresponds to narrower/sharper

focusing bands. Generally, within a certain range of confinement ratios (i.e., $CR = a/H$), the inertial lift forces are scaled as $F_S \propto \rho u_m^2 a^3 / D_h$ and $F_W \propto \rho u_m^2 a^6 / D_h^4$, where ρ is the fluid density, u_m is the maximum fluid velocity, and D_h is the channel hydraulic diameter.[7,40] Therefore, as reported by different groups,[20,41] larger particles should focus more sharply in the microchannels due to stronger inertial forces. As can also be seen in Fig. 3(c), the level of sharpness decreases with the flow rate, but particle size plays a more important role.

1. Commonality #1: Particles tend to gradually approach to the M-M centerline

To evaluate the location of focused particles along the z axis, the channel height needs to be constant at all flow rates. According to our experiments, the original side-view images of different channels show almost a linear trade-off between the maximum expansion of the channel along the z axis and the flow rate (for more information on the channel deformation, see Sec. 5 of the supplementary material). Therefore, we linearly distorted the
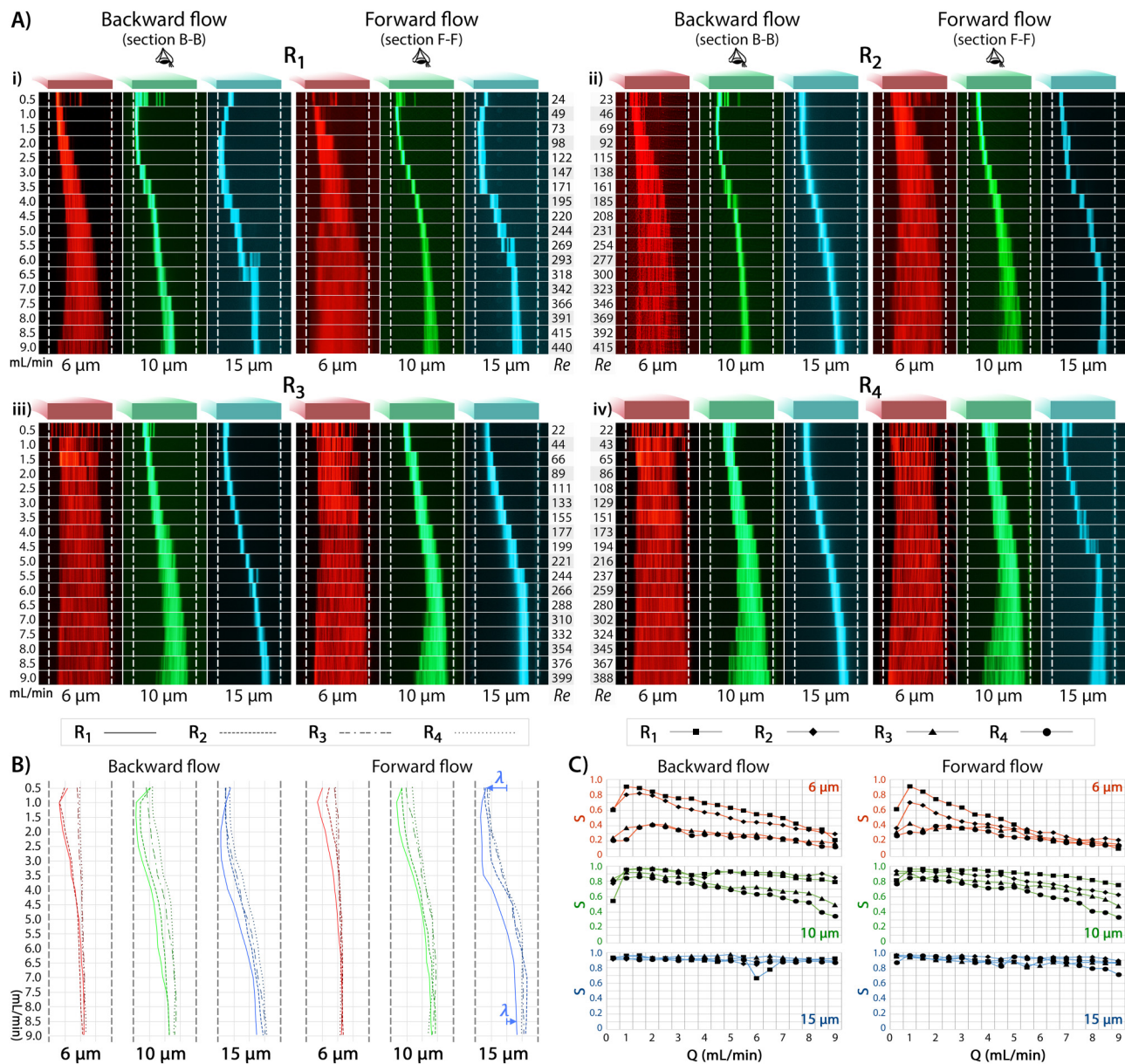
FIG. 3. Experimental results of the rectangular channels. (a) Top-view observations of fluorescent beads of 6, 10, and 15 μm diameter at $Q = 0.5$–9 ml/min in [(i)–(iv)] channels R_{1-4}, respectively. *Note:* The fluorescent color of 6, 10, and 15 μm beads is red, green, and blue, respectively. (b) Focusing positions of microbeads, regardless of how the bands are wide, at $Q = 0.5$–9 ml/min. (c) The sharpness factor for different particle sizes at $Q = 0.5$–9 ml/min.

side-view images of the channel R_1 to account for the deformation of the PDMS-made channel walls [Fig. 4(a)]. The distorted images show that focused particles gradually approach the M-M centerline as the flow rate increases. These results are in agreement with all previously reported observations by other research groups on the macroscale[5,42] and microscale.[43]

2. Commonality #2: A subtle balance exists between the distribution of $\dot{\gamma}$ and F_W

Suspended particles disturb the flow pattern in such a way that when the particles approach the walls, a pressure gradient (i.e., as the origin of F_W) is formed which essentially repels the particle from the wall.[40] On the other hand, F_S, which originates from
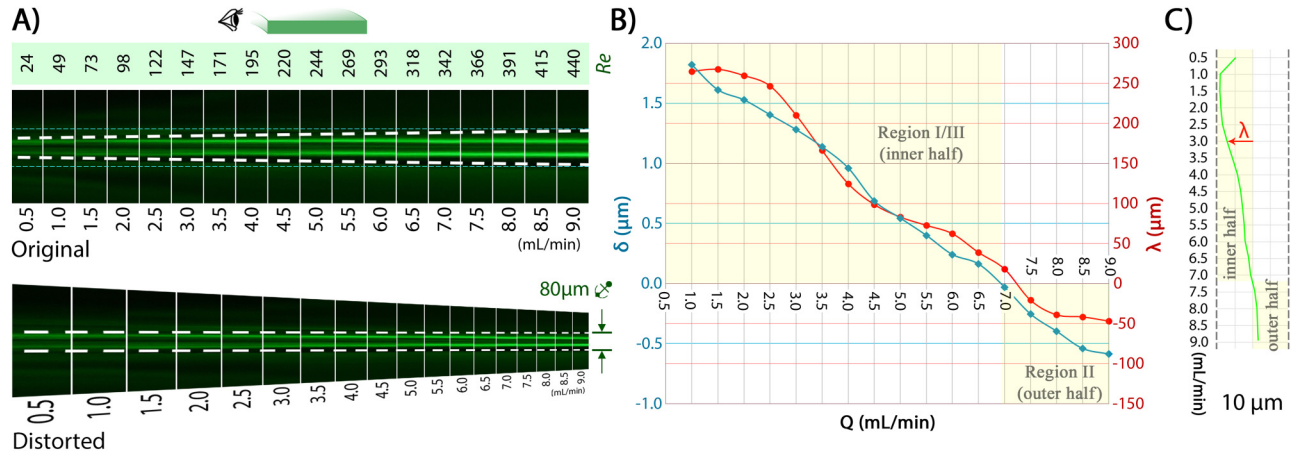
FIG. 4. Approach of particles to the M-M centerline. (a) Original and linearly distorted side-view images of $10\,\mu m$ beads at $Q = 0.5$–9 ml/min in the backward flow of the channel R_1. Very fine dashed blue lines drawn near the top and bottom walls in the original image are horizontal lines. In the distorted image, the channel height is fixed at all the flow rates. (b) Variations of the distance (δ) experimentally measured between the mean of the focusing position of $10\,\mu m$ particles in the channel R_1 and their nearest numerically obtained IPs. λ indicates the distance between the focusing band and the middle of the channel. Note that channel deformation effects inertial focusing and may add error to the measurement of δ, as discussed in Sec. 5 of the supplementary material. (c) The top-view focusing trends of the particles at the same flow rates. Notice that the focusing band switches from the inner half to the outer half at $Q = 7$ ml/min where $\delta \approx 0$.

the shear rate, $\dot{\gamma}$, pushes particles toward the walls. Consequently, as F_S pushes particles more toward the walls, a stronger pressure gradient is formed around the particles, which creates a stronger F_W. Hence, high $-\dot{\gamma}$ regions in the cross section of a channel correspond with regions of high F_W.

Figure 5(a) displays the $\dot{\gamma}$ contours and vectors in the cross section of a rectangular spiral microchannel. Deriving from this figure, Fig. 5(b) provides a schematic of the distribution of high $-\dot{\gamma}$ regions as well as the pattern of secondary flow, which highlights the correspondingly high-F_W regions near the walls.

3. Commonality #3: A curved microchannel consists of three dynamic cross-sectional regions

Flow rate-dependent locations of IPs create a situation where the cross section of the channel can be split into three dynamic regions [i.e., regions I, II, and III displayed in Figs. 5(b) and 5(c)]. In region II, the velocity vectors of Dean flow are outwards, while in regions I and III, the reversed secondary flow drives particles toward the inner wall. This division of the cross section into these three distinct regions is essential as it creates areas where the forces are in balance. F_Ω acts always toward the channel center. Therefore, it is opposed by F_D only in the inner half of regions I and II as well as the outer half of region II [i.e., the "potential focusing areas" highlighted in yellow in Fig. 5(b)]. Outside these areas, F_Ω and F_D are in the same direction, so it is impossible to reach an equilibrium state.
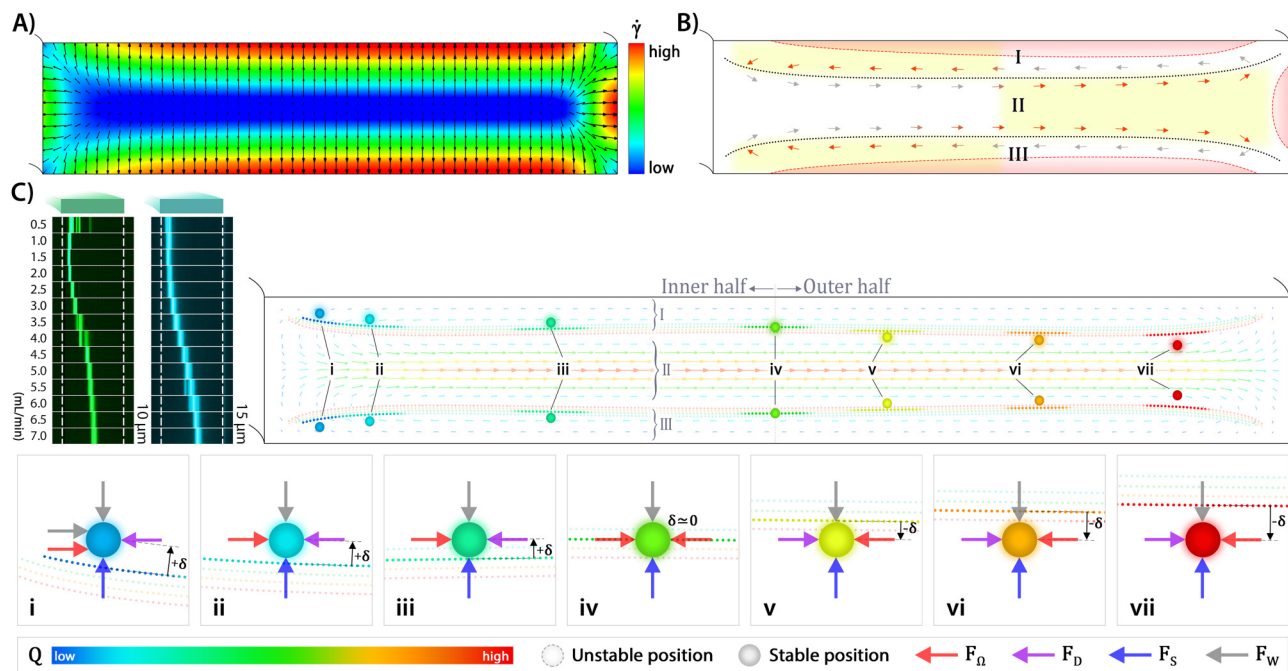
4. Inertial focusing mechanism

The approach of particles to the M-M centerline occurs faster than the relocation of IPs, as is indicated by the dotted lines in Fig. 5(c). Thus, at low flow rates, the equilibrium positions are

situated in regions I and III, i.e., states (i)–(iii), where particles focus due to the local balance of F_Ω and reversed F_D.

The parameter δ is defined as the distance between the focusing position of a particle and its nearest IP. We can also refer to δ as the "influence distance of Dean flow" because larger absolute values of δ correspond to stronger F_D values. This parameter plays a key role in the determination of the force balance as will be discussed below.

As can be seen in Fig. 5(c), in state (i), where the flow rate is very low but high enough (i.e., for microchannels of this study; $Q_{min} > 0.5$ ml/min, $Re > 25$) to allow for inertial focusing,[8,44] δ has a relatively large positive value. In this state, the relatively large magnitude of reversed F_D is strong enough to drag particles nearer to the inner wall where they laterally focus due to the balance of F_W, F_Ω, and the reversed F_D. Upon increasing the flow rate further, δ decreases more and more, i.e., states (ii) and (iii), until state (iv) is reached, where δ becomes approximately zero. In this state, particles experience negligible secondary flow, and their location is governed by F_Ω propelling them to the wall center. By increasing the flow rate beyond this point, δ becomes negative and the equilibrium positions are placed in the outer half of region II. As the flow rate increases, δ takes on a larger negative value and, therefore, particles are exposed to stronger Dean flow which pushes them more toward the outer wall. In states (v) and (vi), particles focus due to the local balance of F_Ω and F_D. Ultimately, in state (vii), δ has a relatively large negative value wherein a relatively large magnitude of F_D is present which drags particles near the outer wall where they are laterally focused due to the balance of F_W, F_Ω, and F_D. This proposed force balance describes why suspended particles in a rectangular channel tend to focus near the inner wall at low flow rates and then gradually shift to the outer side.

FIG. 5. Inertial focusing in rectangular curved channels. (a) $\dot{\gamma}$ contours and vectors. (b) Schematic of the pattern of Dean flow together with the distribution of high $-\dot{\gamma}$ regions (i.e., where $\dot{\gamma} > 90\%$ of $\dot{\gamma}_{max}$) derived from (a). Regions highlighted in yellow indicate the potential focusing areas. Also, regions highlighted in red represent the distribution of F_W areas. (c) Particle equilibrium positions. (i)–(vii) Schematics of the proposed force balances, moving from low to high flow rate, respectively. For ease of comparison, experimental results of the channel R_2 in the backward flow are shown.

To perform a quantitative analysis, we measured δ using both of the empirical and numerical results. Figure 4(b) shows that δ varies (nearly linearly) between $+1.8\,\mu$m at 1 ml/min ($Re = 24$) and $-0.6\,\mu$m at 9 ml/min ($Re = 440$) in the channel R_1 (for more information on the details of the calculations of δ, see Sec. 6 of the supplementary material). Comparing to the corresponding focusing trends observed from the top view [Fig. 4(c)], particles focus in the inner half when δ is positive, reach the middle line of the channel when δ is zero, and focus in the outer half when δ is negative. Also, it can be deduced that there is a close correlation between δ and the top-view focusing distance of particles from the middle of the channel, λ, for any given flow rate [the variations of λ in channels R_{1-4} are shown in Fig. 3(b)]. That is, the lateral position of particles in curved microfluidic channels is determined by δ. This quantitative analysis corroborates with the qualitative force balance discussed above.

Having said that, a work from Papautsky's lab[14] shows that when De exceeds a critical value (De_c), secondary Dean vortices are formed near the outer wall of rectangular spiral microchannels [Fig. 6(a)].[14] The formation of multiple secondary flows affects the particle focusing mechanism. As a result, particles are trapped in the secondary vortices and maintain their position near the outer wall. Nivedita et al.[14] found the magnitude of De_c for three channels with different aspect ratios. To estimate the magnitude of De_c for the rectangular channels of this study, we did a polynomial regression on the reported De_c values. We then
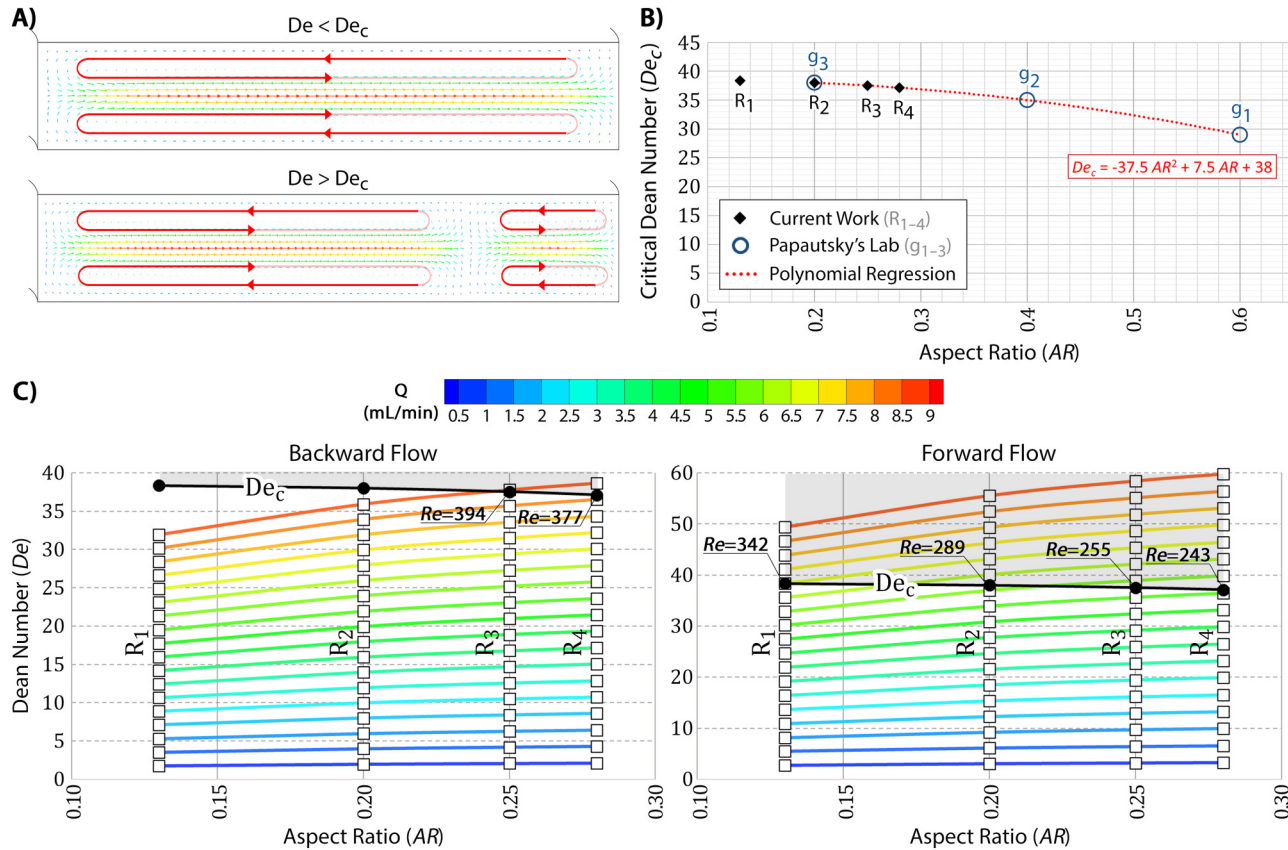
interpolated the De_c for channels R_3 and R_4 and extrapolated it for the channel R_1 using the obtained regression equation, $De_c = -37.5\,AR^2 + 7.5\,AR + 38$ [Fig. 6(b)].

As can be seen in Fig. 6(c), while none of the rectangular channels (R_{1-4}) in the backward flow were affected by the secondary vortices (except for channels R_3 and R_4 at $Q \simeq 9$ ml/min), in the forward flow at relatively high flow rates, multiple secondary flows were expected to have been present. (Note that the trends of Re and De are presented in Sec. 7 of the supplementary material.) To examine the formation of the secondary vortices, we evaluated the experimental results. Figure 3 demonstrates that the lateral migration of particles in the backward flow takes place gradually. In the forward flow, although at $De < De_c$ a gradual migration occurs, at $De > De_c$ particles focus at a relatively constant distance from the outer wall, which implies they are entrapped in the secondary vortices. It is noticeable that there is a perfect match between this behavior of particles and De_c values shown in Fig. 6(c).

5. Effects of the $\dot{\gamma}$ distribution on inertial focusing

As can be noticed in Fig. 5(b), the areas highlighted in red (i.e., high-F_W areas) are thicker in the outer half of the channel, which implies that in curved channels, the $\dot{\gamma}$ distribution tends to have larger values in the outer half. Also, it can be inferred that the distribution of $\dot{\gamma}$ in rectangular channels helps particles stay closer to the M-M centerline at high flow rates.

FIG. 6. Critical Dean number. (a) Schematics of the secondary vortices at $De < De_c$ and $De > D_{ec}$. (b) Interpolation (for channels R_3 and R_4) and extrapolation (for the channel R_1) of D_{ec} using a polynomial regression on the Papautsky's Lab data. (c) Trends of De in backward and forward flows of the rectangular channels of this study. Shaded areas indicate the flow rates where the microchannels are prone to the formation of the secondary vortices.

6. Effects of AR on inertial focusing

Our simulation results (presented in Sec. 8 of the supplementary material) show that generally, excluding near-corner areas of the cross section, the thickness of high $- \dot{\gamma}$ regions (i.e., where F_W is large) is proportional to the channel height. Thus, in channels with higher $AR = H/W$, these areas are thicker (i.e., $R_{4, AR} > R_{3, AR} > R_{2, AR} > R_{1, AR}$). As a result, at the same flow rate particles focus farther from the top and bottom walls so that they are exposed to stronger F_D values. Consequently, (1) particles migrate toward the outer wall at lower flow rates [Fig. 3(b)], and (2) since F_D can exceed F_{Net} when particles get too close to the M-M centerline, particles focus less sharply [Fig. 3(c)]. By this logic, only a certain range of F_D values improve focusing behavior—above or below this range, the secondary flow will be disruptive.

D. Inertial focusing in outward trapezoidal (OT) curved channels

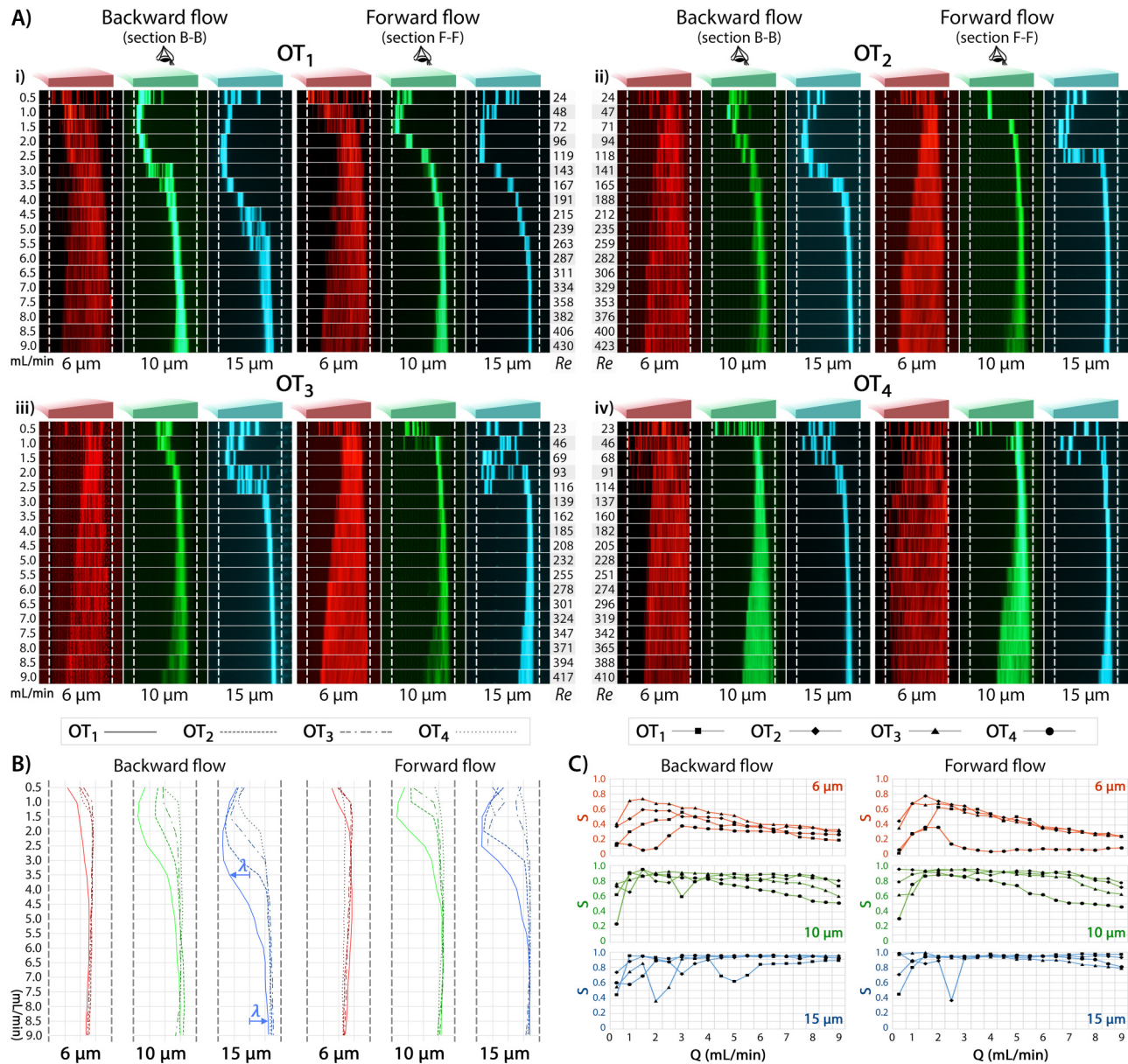The experimental results of channels OT_{1-4} are shown in Fig. 7(a). The focusing trends, λ, and the sharpness values, s, for these channels are presented in Figs. 7(b) and 7(c), respectively. From these results, it can be seen that particles accumulate near the inner wall at low flow rates but migrate to the outer half as Q increases. During this lateral migration, however, 10 and 15 μm particles often undergo a dispersion which results in a dramatic slump in the sharpness factor.

1. Inertial focusing mechanism

The three commonalities of inertial focusing explained in Sec. III C remain much the same in OT channels. Therefore, in states (i) and (ii) shown in Fig. 8(c), δ is positive and particles behave in a similar way to rectangular channels. Having said that, δ has a larger value in state (ii) than (i), which may result in the focus of particles being closer to the inner wall. This behavior can be seen in the trends of 15 μm particles in both forward and backward flows at $Q < 2$ ml/min ($Re < 95$) in channels OT_1 and OT_2.

The focusing behavior at higher flow rates, however, differs from rectangular channels because the IPs are located over oblique curves, neither of which are parallel to the top and bottom walls.

FIG. 7. Experimental results of the OT channels. (a) Top-view observations of fluorescent beads of 6, 10, and 15 μm diameter at $Q = 0.5$–9 ml/min in [(i)–(iv)] channels OT$_{1-4}$, respectively. (b) Focusing positions of microbeads, λ, at $Q = 0.5$–9 ml/min. (c) The sharpness factor for different particle sizes at $Q = 0.5$–9 ml/min.

Thus, at flow rates where a balance between F_S and F_W causes particles to focus very near the IPs, they may actually be located slightly above or below the inflection points, i.e., δ can take on infinitesimally small positive (in the inner half) or negative (in the outer half) values, and particles feel a weak secondary flow along with a local force balance of F_Ω and F_D. Consequently, particles may dissipate and form a relatively wide scattered band in the inner, outer, or both halves of the channel [i.e., state (iii)], e.g., see

the trends of 15 μm particles in both forward and backward flows at $Q < 3$ ml/min ($Re < 138$) in channels OT$_3$ and OT$_4$ in Fig. 7(a).

Furthermore, depending on the slope of the IP curves, focused particles may rapidly cross over the IP locations with a relatively small increase in Q [i.e., state (iv$_1$)]. The entrance of particles into region II in the inner half of the channel will be followed by an abrupt shift to the outer half where F_Ω and F_D become equivalent again [i.e., state (iv$_2$)].
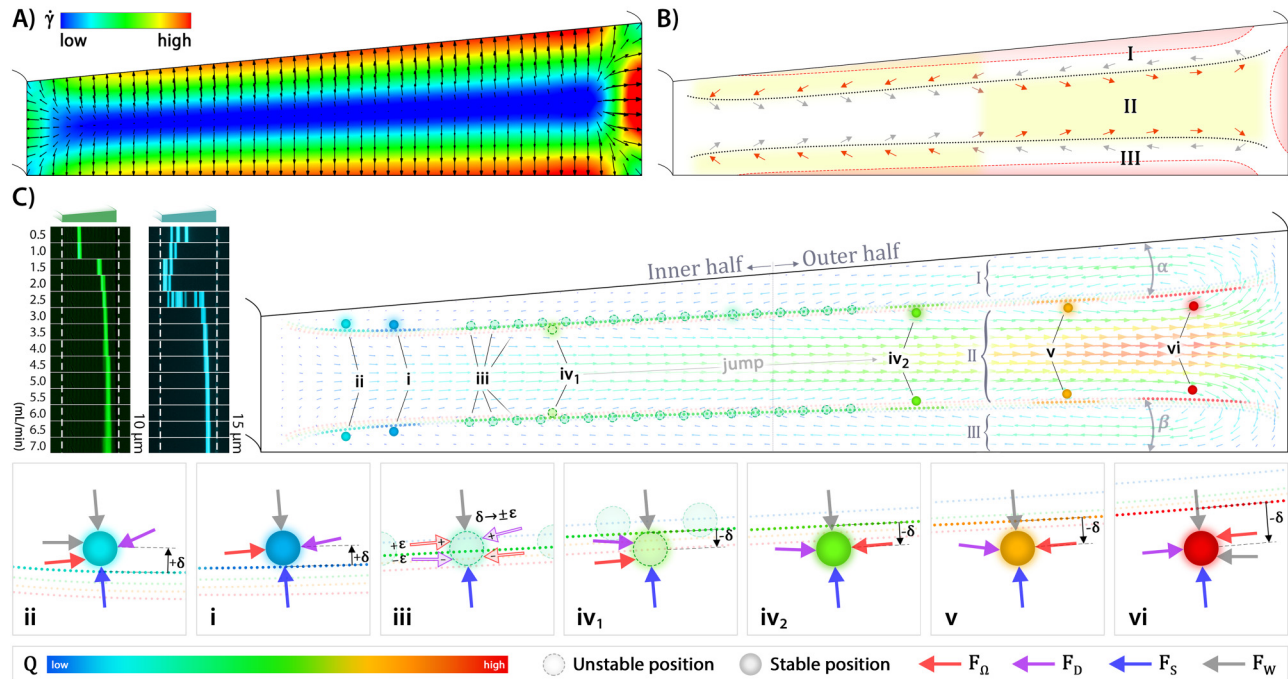
FIG. 8. Inertial focusing in OT curved channels. (a) $\dot{\gamma}$ contours and vectors. (b) Schematics of the pattern of Dean flow as well as the distribution of high $-\dot{\gamma}$ regions (i.e., where $\dot{\gamma} > 90\%$ of $\dot{\gamma}_{max}$) derived from (a). Regions highlighted in yellow indicate the potential focusing areas. Also, regions highlighted in red represent the distribution of high-F_W areas. (c) Particle equilibrium positions. (i)–(vi) Schematics of the proposed force balances, moving from low to high flow rate, respectively. For ease of comparison, experimental results of the channel OT$_2$ in the forward flow are shown.

Lastly, in states (v) and (vi), δ is negative and, therefore, particles focus closer to the outer wall as $|\delta|$ increases with the flow rate. In state (vi), F_W, F_Ω, and F_D are in balance where particles are relatively close to the outer wall.

2. Effects of the Dean flow pattern on inertial focusing

In rectangular microchannels, the majority of the secondary flow vectors are parallel to the top and bottom walls. However, careful observation indicates that the direction of the secondary flow vectors in OT channels is toward region II. Consequently, in the inner half of the channel, particles leave regions I and III and migrate to the outer half at lower flow rates. Also, in the outer half of the channels, this pattern aids particles to stay in region II.

3. Effects of the $\dot{\gamma}$ distribution on inertial focusing

Given the fact that the thickness of high $-\dot{\gamma}$ regions is proportional to the channel height, the general tendency of $\dot{\gamma}$ for having larger values in the outer half of curved channels is amplified by the geometry of OT channels [Fig. 8(a)]. Therefore, according to the second commonality, in OT channels, F_W is much larger in the outer half than that in the inner half [Fig. 8(b)]. This distribution of $\dot{\gamma}$ (i.e., F_W) assists in holding particles in region II at high flow rates.

4. Effects of the wall slope on inertial focusing

As discussed in Sec. III D 3, F_W has a greater magnitude in the outer half of a steeper OT channel. Therefore, F_W pushes particles more forcefully toward region II (i.e., they focus closer to the M-M centerline). Since F_D can exceed F_{Net} in these areas (i.e., as also discussed in Sec. III C 6), the particles focus less sharply [Fig. 7(c)]. Moreover, in a steeper OT channel, the angle between the IP curves and the top and bottom walls is also greater [e.g., angles α and β shown in Fig. 8(c), respectively]. Hence, since state (iv$_1$) must take place at lower flow rates, particles have to leave regions I and III at lower flow rates, which results in an earlier migration of particles to the outer side of the channel [Fig. 7(b)].

E. Inertial focusing in inward trapezoidal (IT) curved channels

The experimental results along with the focusing trends, λ, and the s values for channels IT$_{1-4}$ are shown in Fig. 9. Particles focus close to the inner wall at low flow rates, but gradually migrate toward the outer side with increasing flow rate. This lateral migration is very similar to that in the rectangular channels with the main difference being that particles rarely reach the outer half of IT channels. Moreover, compared to the rectangular and OT channels, particles focus more sharply in IT channels [Fig. 9(c)].
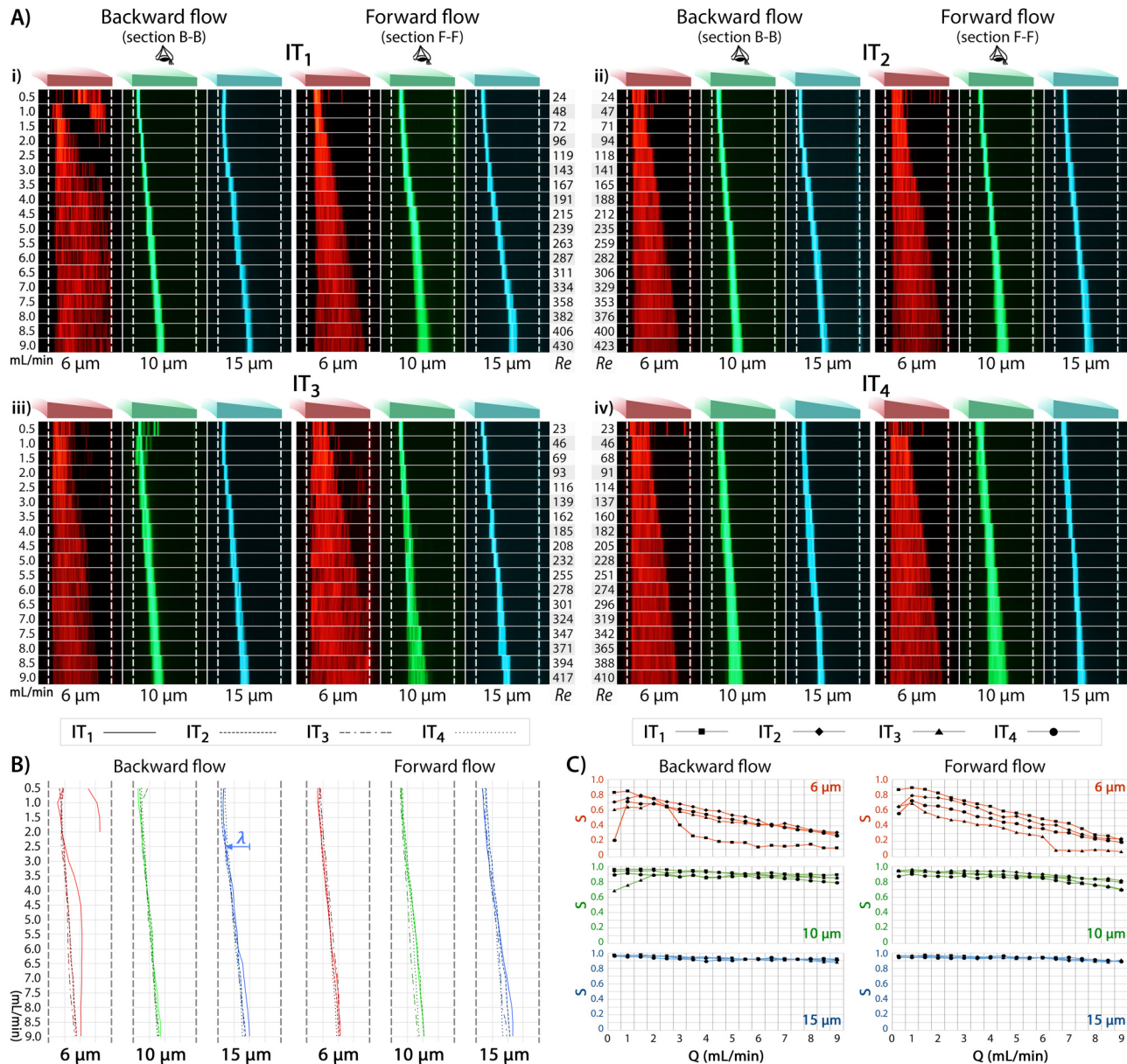
FIG. 9. Experimental results of the IT channels. (a) Top-view observations of fluorescent beads of 6, 10, and 15 μm diameter at $Q = 0.5$–9 ml/min in [(i)–(iv)] channels IT_{1-4}, respectively. (b) Focusing positions of microbeads, λ, at $Q = 0.5$–9 ml/min. (c) The sharpness factor for different particle sizes at $Q = 0.5$–9 ml/min.
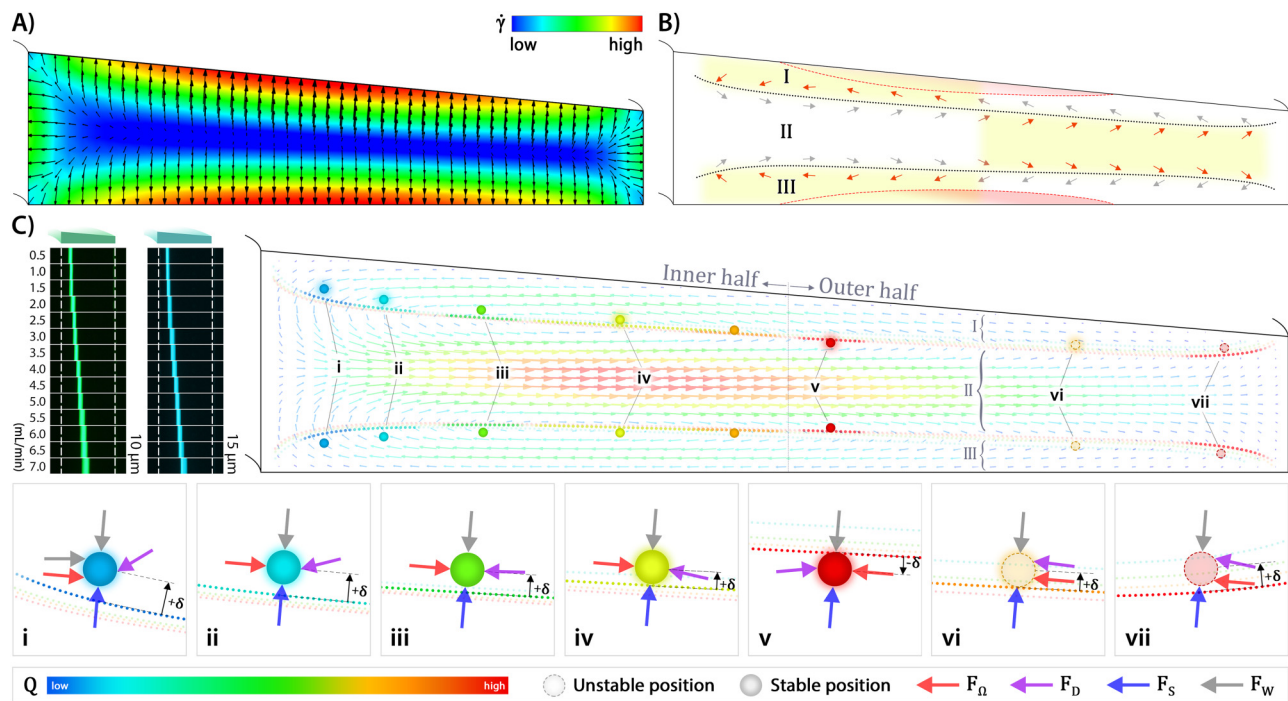
1. Inertial focusing mechanism

The three cross-sectional regions obtained from the third commonality of inertial focusing are shown for IT channels in Fig. 10(b). In the inner half, particles are always placed in regions I and III, while the magnitude of δ decreases gradually with the flow rate [i.e., states (i) to (iv) in Fig. 10(c)]. Therefore, weaker and weaker F_D values counteract F_Ω as the flow rate increases, which is, in fact, the reason behind the lateral migration of particles toward the channel center. At very

high flow rates, depending on the slope of the upper wall, particles may enter region II in the outer half of the channel. However, since they are strongly driven toward regions I and III, particles can only focus very close to the middle of the channel [i.e., state (v)].

2. Effects of the Dean flow pattern on inertial focusing

In IT channels, the direction of the secondary flow vectors is mostly toward regions I and III [Fig. 10(b)]. In the inner half of the

FIG. 10. Inertial focusing in IT curved channels. (a) $\dot{\gamma}$ contours and vectors. (b) Schematics of the pattern of Dean flow as well as the distribution of high $- \dot{\gamma}$ regions (i.e., where $\dot{\gamma} > 90\%$ of $\dot{\gamma}_{max}$) derived from (a). Regions highlighted in yellow indicate the potential focusing areas. Also, regions highlighted in red represent the distribution of high-F_W areas. (c) Particle equilibrium positions. (i)–(vii) Schematics of the proposed force balances, moving from low to high flow rate, respectively. For ease of comparison, experimental results of the channel IT_2 in the forward flow are shown.

channel, F_D opposes F_W and, therefore, with the aid of F_S either keeps particles in regions I and III, or in the unlikely event of the entrance of particles into region II, the resultant of F_D and F_S promptly pushes the particles back to regions I and III. In the outer half of the channel, however, the combination of F_D and F_S does not allow particles to stay in region II, especially the closer particles are to the outer wall [i.e., states (vi) and (vii)]. Therefore, particles predominantly focus in the inner half of the IT channels.

3. Effects of the $\dot{\gamma}$ distribution on inertial focusing

The cross section-independent tendency of $\dot{\gamma}$ for having larger values in the outer half of curved channels is dampened by the geometry of IT channels. Thus, F_W is relatively weak near the outer wall, which gives more freedom to particles to enter regions I and III [Fig. 10(b)]. This distribution of $\dot{\gamma}$, and therefore F_W, assists in keeping particles in regions I and III at all flow rates, which is followed by inertial focusing of particles in the inner half of the channel as these regions do not have any potential focusing areas in the outer half of curved channels.
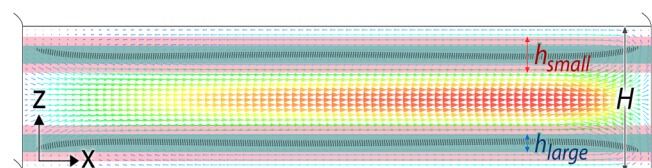
4. Effects of the wall slope on inertial focusing

Since the thickness of high $- \dot{\gamma}$ regions—and thus the distribution of F_W—is proportional to the channel height, δ has a smaller value in state (i) of a steeper IT channel. Therefore, a weaker reversed

F_D acts on particles, which causes them to focus less closely to the inner wall [Fig. 9(b)]. Furthermore, in a steeper IT channel, the angle between the IP curves and the top and bottom walls is greater. Thus, at the same flow rates, δ has a larger value for steeper angles, which is succeeded by a stronger reversed secondary flow. As a result, particles focus more closely to the inner wall in a steeper IT channel [Fig. 9(b)]. In addition, since regions I and III are higher in the inner half of a steeper IT channel, particles focus less sharply [Fig. 9(c)].
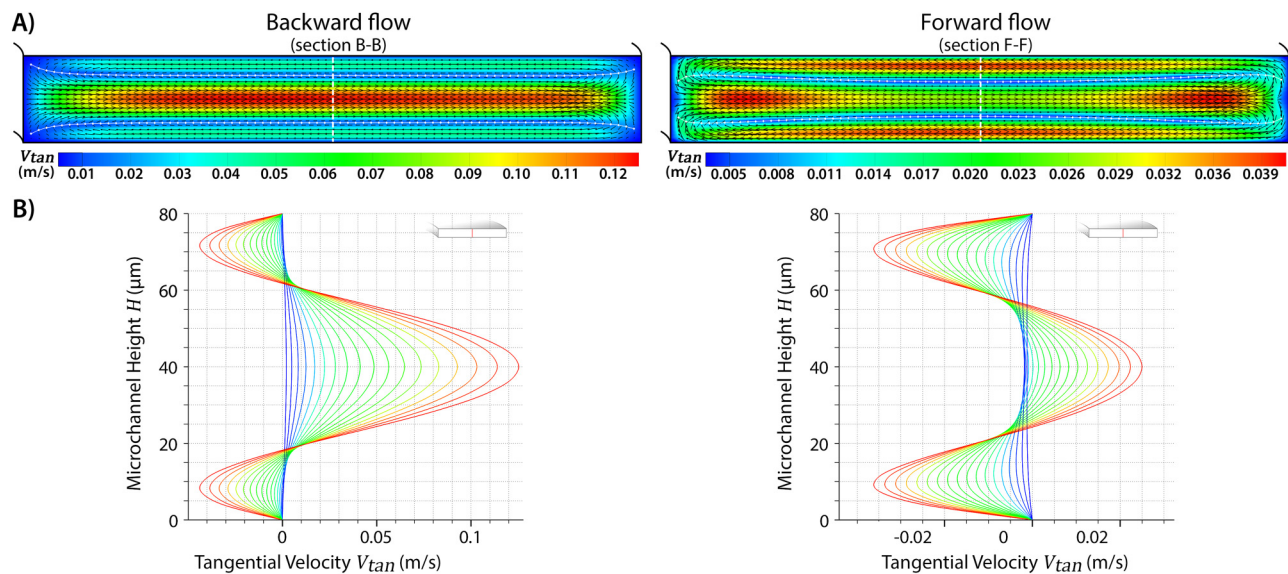
F. General effects of a on inertial focusing

Now that we have discussed rectangular, OT, and IT geometries, it is possible to pull out some general inertial focusing trends. To start, recall that F_D is obtained from Stokes' drag law,[45] where

FIG. 11. Effects of the particle size on inertial focusing. The height of focusing band, h, of small and large particles.

FIG. 12. Effects of the channel curvature on inertial focusing. (a) Comparison of Dean velocity contours (i.e., the pattern of Dean flow) at $Q = 9$ ml/min in the channel R_1 in the backward and forward flows. White dots indicate IPs. (b) Comparison of Dean velocity profiles at $Q = 0.5$–9 ml/min over the vertical white dashed line, shown in (a), in the middle of the channel R_1 in the backward and forward flows.

$F_D = 3\pi\mu a U_D$, with μ representing the fluid dynamic viscosity and U_D providing the magnitude of the secondary flow velocity (i.e., $F_D \propto a$). The rotation-induced lift force scales as $F_\Omega \propto a^3$.[9,46] Also, the resultant of F_S and F_W scales as $F_{SW} \propto a^4$.[8,47]

An analogy between these forces suggests that a reduction of particle size will result in a sharper drop in F_{SW} and F_Ω than in F_D. Thus, smaller particles are more affected by Dean flow which can cause them to exit the potential focusing areas more easily and become fully dispersed. Furthermore, smaller particles are much less influenced by F_{SW} as it has the most dependency on particle size among the forces, i.e., F_S and F_W are mainly influential in locations close to the M-M centerline and the channel walls, respectively. As a result, the value of δ can vary in a wider range for smaller particles—a range which becomes wider and wider as Q increases. Figure 11 demonstrates how the height of the focusing bands, h, changes for particles of different size. Our side-view experimental results of the channels confirm that h for smaller particles is wider than for larger particles at each flow rate (see Sec. 9 of the supplementary material). Moreover, the x-component of the equilibrium position of a particle depends on the magnitude of its δ. Therefore, when particles are free to focus in a wider range of δ, a broader range of equilibrium positions along the channel width is created. This describes why the width of the focusing band, b, for smaller particles is wider than for larger particles (i.e., smaller particles focus less sharply).

G. General effects of R on inertial focusing

Another general effect found in all designs is that the secondary flow pattern changes with the channel's curvature radius R (Fig. 12). Developing a complete understanding of the effect of R on IP

locations would entail another comprehensive study, but since we altered the flow direction to change De in the section of interest, while the rest of parameters including Q and so Re remained unchanged, it is possible to draw some initial relationships.

In the backward flow (i.e., at section B-B), the Dean flow is stronger in region II, while in the forward flow (i.e., at section F-F), the Dean flow is stronger in regions I and III. Although at the same Re, Dean number $De = Re\,(D_h/R)^{-1/2}$ in the forward flow is larger than its value in the backward flow because $R_{F-F} < R_{B-B}$ [Fig. 1(a)], it—by itself—cannot give rise to the difference between the Dean velocity profiles shown in Fig. 12(b). For a certain cross-sectional geometry, we propose that the shape of the Dean velocity profile is a function of φ (Re, De, p, dR/dL), where p and L are pressure and local channel length, respectively. In a spiral microchannel, $dR/dL > 0$ for the backward flow whereas $dR/dL < 0$ for the forward flow.

IV. CONCLUSIONS

In this study, we show that the inflection points of the secondary flow are not fixed, as is commonly purported. Rather, these points are a function of the flow rate and geometry. We propose that relaxing this assumption of fixed inflection points enables a full fundamental understanding of the complex focusing behavior in curved microchannels—one which encompasses several previously unexplained phenomena.

The backbone of the proposed theory consists of three commonalities: (1) particles gradually approach the M-M centerline as the flow rate increases; (2) the distribution of shear rate corresponds to the magnitudes of wall-induced lift force; (3) all the possible focusing areas within the cross section of any curved channel are determined through division of the cross section into three

regions—regions that are defined based on the dynamic locations of inflection points of Dean flow. From these commonalities, it is possible to put the mechanisms of inertial focusing in microchannels in perspective with different cross-sectional shapes.

The influence distance of Dean flow (δ) plays a key role in the explanation of particle states, since it allows us to elucidate the force balance in each focusing state. The numerical and experimental findings investigated herein all support the "inflection point displacement theory" proposed in this paper. That is, for a certain cross-sectional geometry, we can conclude that the magnitude of this parameter takes the form of $\delta = \delta\,(\dot{\gamma}, \varphi, a)$ because it is influenced by both the axial and Dean velocity profiles as well as the particle size. The distribution of $\dot{\gamma}$ is directly obtained from the axial velocity profile, while φ represents the shape of the Dean velocity profile.

For rectangular curved channels, δ clearly explains why particles focus near the inner wall at low flow rates and then migrate laterally toward the outer wall as the flow rate increases. For outward trapezoidal channels, the proposed theory describes why focusing bands either dissipate or abruptly shift from the inner half to the outer half of the channel, as has been observed—but not explained—in the literature. Also, δ helps explain the focusing behavior of particles in inward trapezoidal channels, where particles predominately focus in the inner half of the channel.

Furthermore, this logic sheds light on the effects of different parameters on inertial focusing, including flow rate, particle size, aspect ratio, wall slope, wall slope direction, curvature radius, flow direction, shear rate distribution, and Dean flow pattern. Overall, we believe that these new insights for the particle focusing mechanisms in rectangular and trapezoidal curved channels will open the door to better design optimization and many more novel microfluidic devices which incorporate compound cross-sectional shapes for improved microparticle/cell manipulation.[48]

V. METHODS

A. Design and microfabrication

All of the spiral microchannels were designed in SolidWorks,® and then made of polydimethylsiloxane polymer (PDMS, Sylgard 184 Silicone Elastomer Kit, Dow Corning) using soft lithography. The positive print of the microchannels were precisely milled of aluminum using micromilling (Whits Technologies, Singapore, and BioMEMS Supply, Sydney, Australia). Degassed PDMS, mixed in a 10:1 ratio of the base and the curing agent, was poured into the manufactured aluminum molds and peeled off after prebaking for 2 h inside an oven at 65 °C. Fluidic access holes were punched using a Uni-Core™ Puncher with a diameter of 1.5 mm (Sigma-Aldrich Co. LLC, SG). The device was then irreversibly bonded with a flat, thick PDMS slab using an oxygen plasma unit (PDC-002, Harrick Plasma, Ossining, NY). Finally, the fabricated microchips were left 2 h in the oven for postbaking at 65 °C to ensure consistency amongst the different microchips.

B. Bead suspensions

Fluorescently labeled microbeads (Fluoresbrite® Microspheres, Polysciences Inc., Singapore) with diameters of 6, 10, and 15 μm were added (@ 0.01% volume fraction) to individual sample buffers (i.e., MACS buffers) consisting of 1× phosphate buffered saline (PBS), 2 mM EDTA supplemented with 0.5% bovine serum albumin (BSA), and 0.09% Azide (Miltenyi Biotec, Germany). MCAS buffer was used to prevent nonspecific adhesion of microbeads to the tubing and microchannel walls.

C. Experimental setup

The spiral microfluidic devices were mounted on an inverted phase contrast/epifluorescence microscope (Olympus IX73 microscope, Olympus Inc., USA) equipped with a DP80 dual chip CCD camera (Olympus Inc., USA). The exposure time and sensitivity were set to 50 ms and ISO 800-1600, respectively, to ensure a fast shutter speed. The bead suspensions were loaded into BD plastic 10 ml syringes with a Luer-Lok® tip and pumped through the microchannels at varying flow rates ranging from 0.5 to 9 ml/min ($Re \approx 22$ to 440). In order to automate the pumping process, a programmable syringe pump (Chemyx Fusion 200, Chemyx Inc., USA) was used. The syringe pump was programed to keep the initial flow rate for 25 s and then increase the flow rate every 5 s with the step size of 0.5 ml/min. Next, TechSmith® Camtasia Studio® was used to record the screen. The recordings were then rendered as full frame (i.e., uncompressed) Audio Video Interleave (AVI) video files at 30 fps. Frames taken from the video files were compared with images acquired by cellSens software (Olympus Inc., USA) to certify the quality of the extracted frames.

D. Numerical simulations

ANSYS-FLUENT® 16.0-18.0 was used for the numerical simulation of an incompressible laminar flow in the spiral microchannels at the same 18 different flow rates in both of the forward and backward directions. Constant velocity inlet and atmospheric pressure outlet were used as boundary conditions. Also, the no-slip boundary condition was used at the walls. The fluid was assumed to be liquid water at 20 °C with density and viscosity of 998.2 kg/m³ and 1.003×10^{-3} kg/m s, respectively. The SIMPLE scheme was used as the pressure-based segregated algorithm for steady-state calculations with the pressure–velocity coupling method. The grid size was determined via a mesh independence study to be fine enough (i.e., fully hexahedral grids with the minimum height of 2 μm and with the maximum height of 4 μm) to assure accurate numerical results.

A high-performance computing facility was used for the numerical computations. After simulation, FLUENT® journal files were created to export Tecplot® data files for planes corresponding to sections F-F and B-B. Finally, Tecplot® macrofiles were dynamically created by a software application developed in this work to automate the process of generating graphs.

SUPPLEMENTARY MATERIAL

See the supplementary material document that contains information about geometric parameters of the microchannels, developed software applications, image processing, video processing, channel deformation, measurement of δ, trends of Re and De, shear distribution, and side-view experimental results.

REFERENCES

[1] A. Manz, D. J. Harrison, E. M. Verpoorte, J. C. Fettinger, A. Paulus, H. Lüdi, and H. M. Widmer, J. Chromatogr. A **593**, 253–258 (1992).

[2] J. Zhang, S. Yan, D. Yuan, G. Alici, N.-T. Nguyen, M. E. Warkiani, and W. Li, Lab Chip **16**, 10–34 (2016).

[3] M. S. Syed, M. Rafeie, D. Vandamme, M. Asadnia, R. Henderson, R. A. Taylor, and M. E. Warkiani, Bioresour. Technol. **252**, 91–99 (2017).

[4] B. C. Syverud, E. Lin, S. Nagrath, and L. M. Larkin, Tissue Eng. C Methods **24**, 32–41 (2018).

[5] J.-P. Matas, J. F. Morris, and É. Guazzelli, J. Fluid Mech. **515**, 171–195 (2004).

[6] D. Di Carlo, D. Irimia, R. G. Tompkins, and M. Toner, Proc. Natl. Acad. Sci. U.S.A. **104**, 18892–18897 (2007).

[7] D. Di Carlo, J. F. Edd, K. J. Humphry, H. A. Stone, and M. Toner, Phys. Rev. Lett. **102**, 094503 (2009).

[8] D. Di Carlo, Lab Chip **9**, 3038–3046 (2009).

[9] J. Zhou and I. Papautsky, Lab Chip **13**, 1121–1132 (2013).

[10] A. J. Mach and D. Di Carlo, Biotechnol. Bioeng. **107**, 302–311 (2010).

[11] M. Masaeli, E. Sollier, H. Amini, W. Mao, K. Camacho, N. Doshi, S. Mitragotri, A. Alexeev, and D. Di Carlo, Phys. Rev. X **2**, 031017 (2012).

[12] W. Dean, Lond. Edinb. Dublin Philos. Mag. J. Sci. **4**, 208–223 (1927).

[13] H. Ramachandraiah, S. Ardabili, A. M. Faridi, J. Gantelius, J. M. Kowalewski, G. Mårtensson, and A. Russom, Biomicrofluidics **8**, 034117 (2014).

[14] N. Nivedita, P. Ligrani, and I. Papautsky, Sci. Rep. **7**, 44072 (2017).

[15] F. Liu, D. Zhang, Y. Cai, Z. Qiu, Q. Zhu, J. Zhao, L. Wang, and H. Tian, Int. J. Heat Mass Transf. **129**, 534–546 (2019).

[16] S. C. Ray and R. N. Mondal, Am. Sci. Res. J. Eng. Technol. Sci. **46**, 71–99 (2018).

[17] Z. Liu, M. Li, Y. Pang, L. Zhang, Y. Ren, and J. Wang, Phys. Fluids **31**, 022004 (2019).

[18] S. L. Stott, C.-H. Hsu, D. I. Tsukrov, M. Yu, D. T. Miyamoto, B. A. Waltman, S. M. Rothenberg, A. M. Shah, M. E. Smas, and G. K. Korir, Proc. Natl. Acad. Sci. U.S.A. **107**, 18392–18397 (2010).

[19] W. Li, S. Yan, R. Sluyter, N.-T. Nguyen, J. Zhang, and G. Alici, Sci. Rep. **4**, 4527 (2014).

[20] D. Di Carlo, D. Irimia, R. G. Tompkins, and M. Toner, Proc. Natl. Acad. Sci. U.S.A. **104**, 18892–18897 (2007).

[21] J. Zhang, D. Yuan, Q. Zhao, A. J. Teo, S. Yan, C. H. Ooi, W. Li, and N.-T. Nguyen, Anal. Chem. **91**(6), 4077–4084 (2019).

[22] J.-S. Park, S.-H. Song, and H.-I. Jung, Lab Chip **9**, 939–948 (2009).

[23] D. Jiang, D. Huang, G. Zhao, W. Tang, and N. Xiang, Microfluid. Nanofluidics **23**, 7 (2019).

[24] H. Amini, E. Sollier, M. Masaeli, Y. Xie, B. Ganapathysubramanian, H. A. Stone, and D. Di Carlo, Nat. Commun. **4**, 1826 (2013).

[25] J. Seo, M. H. Lean, and A. Kole, Appl. Phys. Lett. **91**, 033901 (2007).

[26] M. E. Warkiani, L. Wu, A. K. Tay, and J. Han, Annu. Rev. Biomed. Eng. **17**, 1–34 (2015).

[27] J. M. Martel and M. Toner, Phys. Fluids **24**, 032001 (2012).

[28] L. Wu, G. Guan, H. W. Hou, A. A. S. Bhagat, and J. Han, Anal. Chem. **84**, 9324–9331 (2012).

[29] G. Guan, L. Wu, A. A. Bhagat, Z. Li, P. C. Chen, S. Chao, C. J. Ong, and J. Han, Sci. Rep. **3**, 1475 (2013).

[30] M. E. Warkiani, G. Guan, K. B. Luan, W. C. Lee, A. A. S. Bhagat, P. K. Chaudhuri, D. S.-W. Tan, W. T. Lim, S. C. Lee, and P. C. Chen, Lab Chip **14**, 128–137 (2014).

[31] M. E. Warkiani, A. K. P. Tay, G. Guan, and J. Han, Sci. Rep. **5**, 11018 (2015).

[32] M. Rafeie, J. Zhang, M. Asadnia, W. Li, and M. E. Warkiani, Lab Chip **16**, 2791–2802 (2016).

[33] N. Xiang, X. Shi, Y. Han, Z. Shi, F. Jiang, and Z. Ni, Anal. Chem. **90**, 9515–9522 (2018).

[34] W. Lee, D. Kwon, W. Choi, G. Y. Jung, A. K. Au, A. Folch, and S. Jeon, Sci. Rep. **5**, 7717 (2015).

[35] S. Sofela, S. Sahloul, M. Rafeie, T. Kwon, J. Han, M. E. Warkiani, and Y.-A. Song, Lab Chip **18**, 679–687 (2018).

[36] J. Sun, M. Li, C. Liu, Y. Zhang, D. Liu, W. Liu, G. Hu, and X. Jiang, Lab Chip **12**, 3952–3960 (2012).

[37] A. Özbey, M. Karimzadehkhouei, S. Akgönül, D. Gozuacik, and A. Koşar, Sci. Rep. **6**, 38809 (2016).

[38] D. H. Yoon, J. B. Ha, Y. K. Bahk, T. Arakawa, S. Shoji, and J. S. Go, Lab Chip **9**, 87–90 (2009).

[39] J. M. Martel and M. Toner, Sci. Rep. **3**, 3340 (2013).

[40] J. M. Martel and M. Toner, Annu. Rev. Biomed. Eng. **16**, 371–396 (2014).

[41] N. Xiang, Z. Shi, W. Tang, D. Huang, X. Zhang, and Z. Ni, RSC Adv. **5**, 77264–77273 (2015).

[42] J. Matas, J. Morris, and E. Guazzelli, Oil Gas Sci. Technol. **59**, 59–70 (2004).

[43] A. T. Ciftlik, M. Ettori, and M. A. Gijs, Small **9**, 2764–2773 (2013).

[44] J. Oakey, R. W. Applegate, Jr., E. Arellano, D. D. Carlo, S. W. Graves, and M. Toner, Anal. Chem. **82**, 3862–3867 (2010).

[45] S. S. Kuntaegowdanahalli, A. A. Bhagat, G. Kumar, and I. Papautsky, Lab Chip **9**, 2973–2980 (2009).

[46] S. Rubinow and J. B. Keller, J. Fluid Mech. **11**, 447–459 (1961).

[47] E. S. Asmolov, J. Fluid Mech. **381**, 63–87 (1999).

[48] M. Rafeie, S. Hosseinzadeh, J. Huang, A. Mihandoust, M. E. Warkiani, and R. A. Taylor, Biomicrofluidics **13**, 034118 (2019).